NANO LETTERS

pubs.acs.org/NanoLett Letter

Closed Pore Architecture and Sodium Cluster Deposit Visualization in Hard Carbon

Bobo Sun,[▽] Ruohan Yu,[▽] Yuxia Zhong, Jinshuai Liu, Zihe Wei, Xia Wang, Guangwan Zhang, Meng Huang, Lei Zhang, Qin Wang, Fei Lv, and Liang Zhou*

Cite This: *Nano Lett.* 2025, 25, 7161−7169 Read Online

ACCESS | Metrics & More | Article Recommendations | Supporting Information

ABSTRACT: Achieving the full potential of hard carbon (HC) for sodium storage requires a deep understanding of its complex porous structure as well as charge storage mechanism. While the contribution of sodium deposition within HC pores to the overall capacity is recognized, detailed visualization and mechanistic understanding of this process remain challenging. This study leverages advanced electron microscopy techniques to probe the intricate pore architecture of HC and directly visualize sodium storage within its pores. By employing an HC material (PHC-1) with rich closed pores as the platform material, electron tomography is utilized to reconstruct the pore architecture of PHC-1, providing quantitative insights into porosity, pore size, and pore structure. Low-dose electron microscopy visualizes metastable sodium clusters filling up within the pores during sodiation. Complementary in-situ and ex-situ characterizations further elucidate the synergistic adsorption-intercalation-filling mechanism of PHC-1. This contribution provides significant insights into the structure−property correlation of HC.

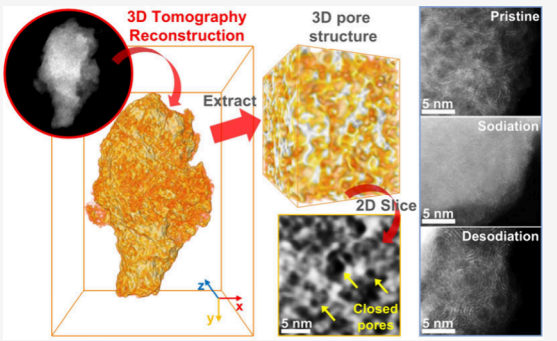

KEYWORDS: *hard carbon anode, sodium-ion batteries, closed pore, 3D structural reconstruction, sodium cluster*

The growing need for sustainable and cost-effective energy storage has positioned sodium-ion batteries (SIBs) as a viable choice, primarily due to the low cost and great abundance of sodium.[1−3] Unlike lithium-ion batteries (LIBs), which utilize graphite anodes, SIBs require alternative anode materials, because of the thermodynamic instability of sodium−graphite intercalation compounds.[4−6] This has driven extensive research into a range of potential anode materials, with hard carbon (HC) emerging as a highly promising candidate, due to its substantial sodium storage capacity and suitable operating potential.[7−9]

The sodium storage property of HC is closely linked to its microstructure, which is characterized by fine, few-layer, curved graphene sheets that are stacked in a disordered manner, forming a semicrystalline structure with a high density of defects and pores.[10,11] This distinctive architecture supports a complex sodium storage mechanism that includes Na^+ adsorption on surfaces and defect sites, Na^+ insertion in graphene layers, and, importantly, the filling of nanopores with electrochemically deposited sodium.[12−14] The electrochemical profile of HC anodes is typically characterized by a sloping region above 0.1 V, corresponding to Na^+ adsorption and insertion, and a plateau region below 0.1 V, associated with closed nanopore filling by quasi-metallic Na cluster.[15] It is well-established that this low-voltage plateau capacity, a major contributor to the overall capacity, is directly correlated with the porosity, pore size, and accessibility of the closed nanopores.[16−18]

Therefore, the rational design of high-performance HC anodes is contingent upon precise control over their porous architecture.[19−21] To this end, considerable effort has been invested in developing synthesis techniques, such as the use of triblock copolymer templates to tailor the porosity of HC.[22,23] However, fully understanding the interplay between closed nanopores and sodium storage requires a direct correlation between the complex three-dimensional (3D) porous architecture and the distribution of Na clusters within the pores. This remains a challenge due to limitations inherent in conventional characterization techniques.

Herein, a hard carbon material with rich closed pores (designated PHC-1) has been constructed as the platform material to study its detailed pore architecture and sodium storage mechanism. Leveraging the capabilities of electron tomography, we reconstruct the intricate porous architecture of PHC-1 in three dimensions, providing quantitative data on

Received: March 12, 2025
Revised: April 12, 2025
Accepted: April 14, 2025
Published: April 16, 2025

https://doi.org/10.1021/acs.nanolett.5c01616
Nano Lett. 2025, 25, 7161−7169

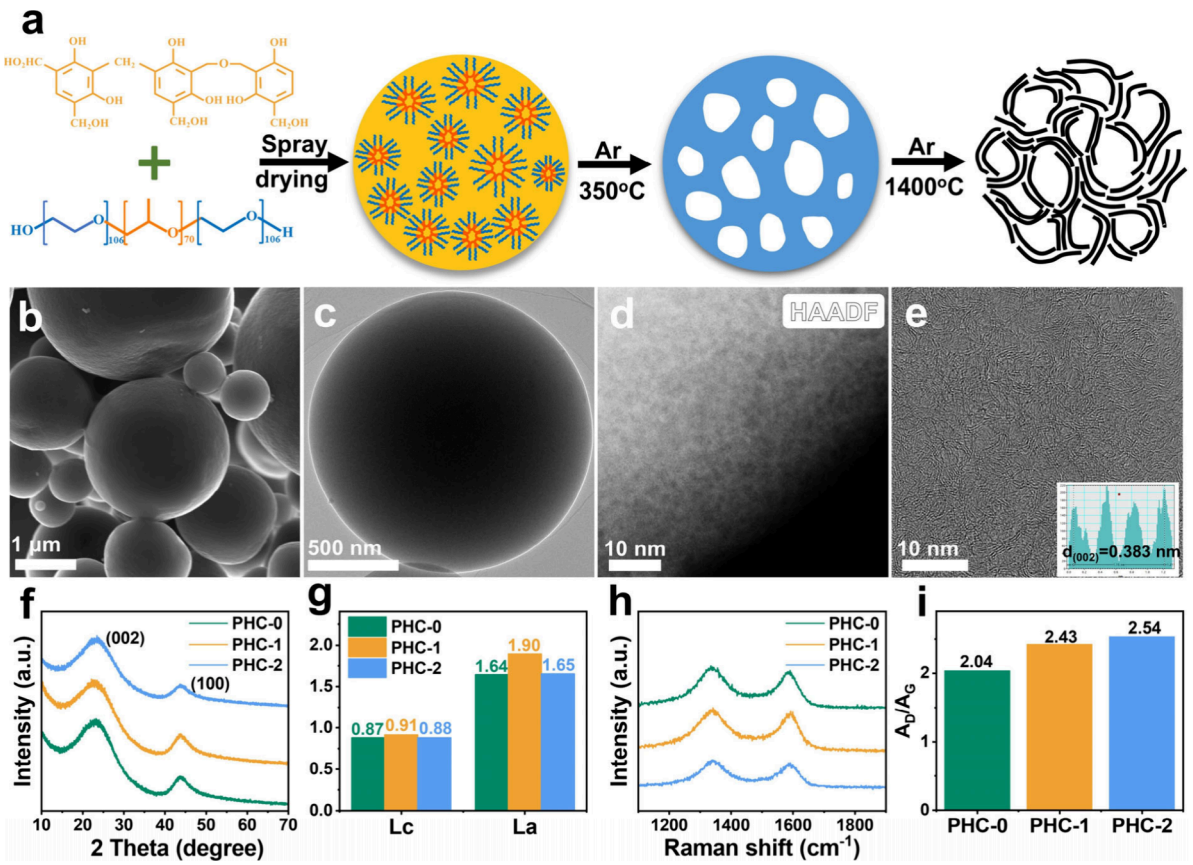

Figure 1. Microstructure of the customized HC. (a) Schematic illustration of the synthesis of PHC-1; (b) SEM image of PHC-1; (c) TEM image of PHC-1; (d) HAADF-STEM image of PHC-1; (e) HRTEM image of the PHC-1; (f, g) XRD patterns (panel (f)) and the corresponding graphitic crystallite size (panel (g)) of PHC-0, PHC-1, and PHC-2; (h, i) Raman spectra (panel (h)) and the corresponding D-band to G-band areal ratio (panel (i)) of PHC-0, PHC-1, and PHC-2.

the porosity, pore size, and pore structure. Furthermore, low-dose electron microscopy based on aberration-corrected transmission electron microscopy (AC-TEM) is employed to directly visualize the spatial distribution of sodium clusters within the closed pores of PHC-1 after sodiation, providing unambiguous evidence of sodium deposition within the confined nanospaces. These advanced imaging techniques, coupled with comprehensive electrochemical characterization and complementary in-situ and ex-situ studies, allow us to elucidate the interplay between the complex porous architecture and the sodium storage mechanism of HC materials. This contribution not only provides a thorough understanding of the sodium storage in the closed pores of HC but also provides insights on the rational design of advanced HC materials for SIBs.

The platform materials, hard carbon microspheres, were synthesized by a soft template-assisted spray drying method (Figure 1a). In detail, a mixture containing phenolic resin, serving as the carbon precursor, and Pluronic F127 (0, 1, 2 g), serving as the porogen, were spray-dried to form composite microspheres. The presence of F127 within the composite microspheres was confirmed by Fourier transform infrared (FTIR, Figure S1a), and its decomposition during pyrolysis at 350 °C under Ar was verified by thermogravimetric analysis (TGA, Figure S1b). Final high-temperature carbonization under an Ar atmosphere yielded HC materials (PHC-0, PHC-1, PHC-2) with tailored porosity.

Scanning electron microscopy (SEM) and transmission electron microscopy (TEM) reveal that both PHC-0 (Figure S2) and PHC-1(Figures 1b and 1c) exhibit a smooth spherical morphology, whereas PHC-2 (Figure S3) displays a collapsed spherical shape with a roughened surface. High-angle annular dark-field scanning transmission electron microscopy (HAADF-STEM) reveals that PHC-1 (Figure 1d) contains a more uniform distribution of pores within the carbon matrix compared to PHC-0 and PHC-2 (Figure S4). High-resolution TEM (HRTEM) images of PHC-1 (Figure 1e) show numerous closed pores surrounded by randomly oriented and tightly stacked graphitic carbon layers, with an interlayer spacing of approximately 0.38 nm. For PHC-0 and PHC-2, they exhibit fewer closed pores (Figure S5).

X-ray diffraction (XRD) patterns of the PHC samples (Figure 1f) display broad diffractions characteristic of HC at ~23° and 45°, corresponding to the (002) and (100) planes, respectively. The (002) peak shifts to lower angles with increasing F127 content, indicating an increase in interlayer spacing, as calculated by the Bragg equation. The average crystallite thickness (L_c) along the *c*-axis and width (L_a) along the *a*-axis are determined by the Scherrer equation: L_c = 0.87, 0.91, and 0.88 nm; L_a = 1.64, 1.90, and 1.65 nm for PHC-0, PHC-1, and PHC-2, respectively (Figure 1g).[16,24]

X-ray photoelectron spectroscopy (XPS) confirms that all samples are primarily composed of carbon (C) and oxygen (O) (Figure S6). High-resolution C 1s spectra show components at around 284.8, 285.7, 287.1, and 289.0 eV,

https://doi.org/10.1021/acs.nanolett.5c01616
Nano Lett. 2025, 25, 7161−7169

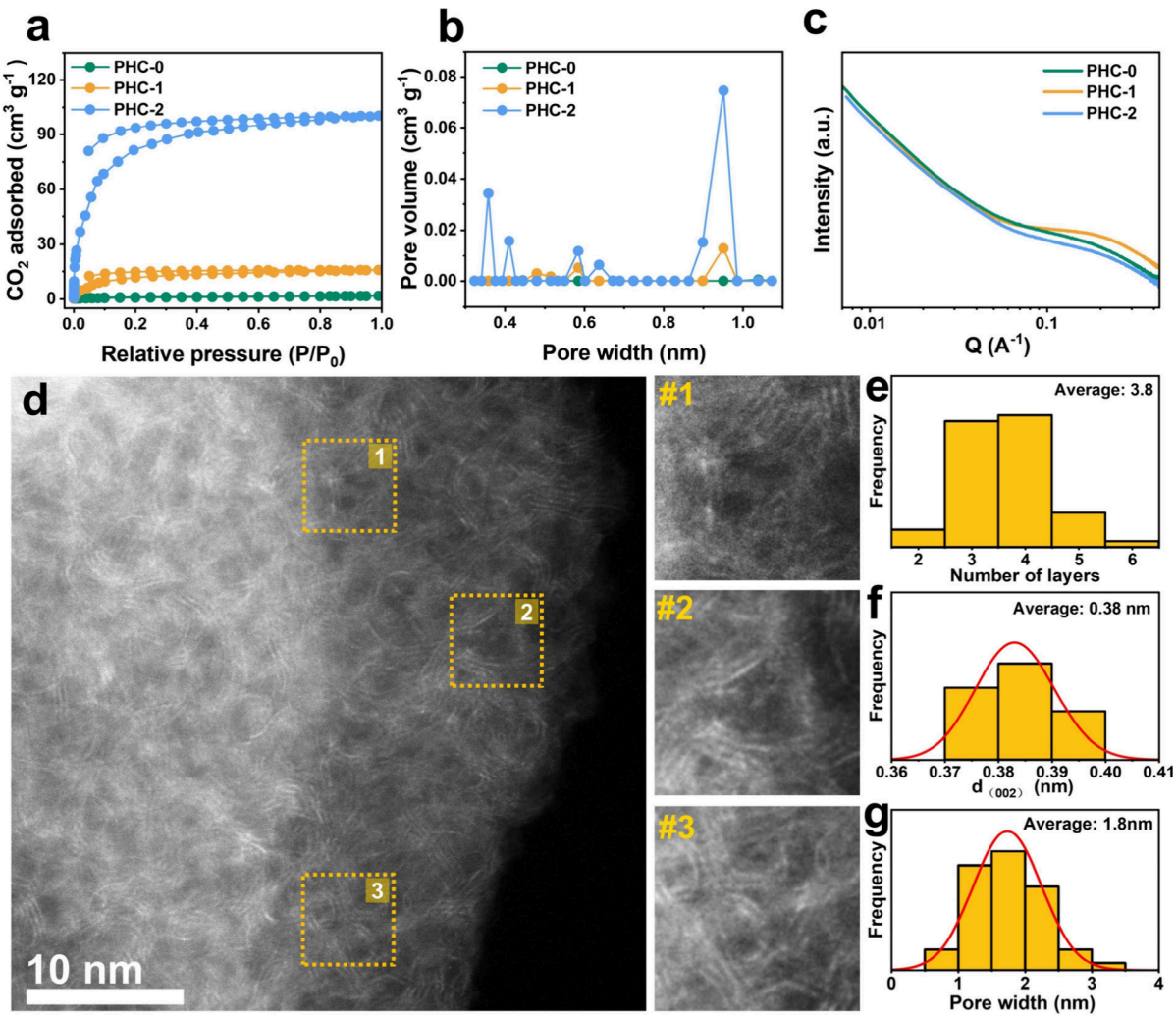

Figure 2. Porous architecture characterization. (a, b) CO_2 adsorption−desorption isotherms (panel (a)) and the corresponding pore size distributions (panel (b)) of PHC-0, PHC-1, and PHC-2; (c) SAXS patterns of PHC-0, PHC-1, and PHC-2; (d) HAADF-STEM image and the corresponding enlarged images of PHC-1; (e, f, g) statistical illustration of the stacked carbon layers (panel (e)), interlayer spacing (panel (f)), and pore diameter of PHC-1 (panel (g)).

which are assigned to C−C, C−O, C═O, and O−C═O bonds, respectively.[25] The CHONS analysis results show that the O content generally increases as the F127 dosage increases (Table S1). Raman spectroscopy (Figures 1h, 1i) reveals an increasing of the D-band to G-band ratio (A_D/A_G) from 2.04 for PHC-0 to 2.54 for PHC-2. That is to say, a greater amount of F127 would induce a higher degree of disorder (Figure S7).[26]

To investigate the influence of F127 on the porous structure of HC materials, N_2 adsorption−desorption isotherms are obtained for PHC-0, PHC-1, and PHC-2 (Figure S8a). Brunauer−Emmett−Teller (BET) analysis shows specific surface areas of 2.9, 4.3, and 226.2 $m^2\ g^{-1}$ for PHC-0, PHC-1, and PHC-2, respectively. The low surface area of PHC-1 unambiguously demonstrates its closed pore structure. Pore size distributions (Figure S8b) indicate a lack of significant pores in PHC-0 and PHC-1, while the PHC-2 exhibits pores primarily in the 2−7 nm range.

To further probe the micropores, we conducted CO_2 adsorption−desorption measurements (Figure 2a). The PHC-2 exhibits a substantially higher CO_2 uptake than PHC-0 and PHC-1, confirming its greater pore volume (Figure 2b). With rich micropores ranging from 0.3 to 0.9 nm, PHC-2 has a pore volume of 0.18 $cm^3\ g^{-1}$. In contrast, PHC-0 and PHC-1 show minimal CO_2 adsorption, with calculated pore volumes of only 0.0029 and 0.028 $cm^3\ g^{-1}$, respectively. Therefore, both N_2 and CO_2 sorption results show that PHC-2 has a different pore structure compared to PHC-0 and PHC-1. Although both PHC-1 and PHC-2 are templated from F127, it is postulated that the pores in PHC-1 might be predominantly closed and thus inaccessible to N_2.[16] To verify this hypothesis, small-angle X-ray scattering (SAXS) is employed to probe the closed pore structure, as SAXS is able to detect both open and closed pores. The SAXS patterns (Figure 2c) exhibit characteristic scattering features in the 0.01−1 $Å^{-1}$ region, indicative of nanoporosity. Notably, the PHC-1 displays a marked increase in scattering intensity within the region compared to PHC-0 and PHC-2, suggesting a significantly higher amount of closed pores.[27]

Detailed analysis of the SAXS data (Figure S9a−c) allows for the determination of closed pore parameters. The average closed pore size in PHC-1 is estimated to be 2.5 nm (Figure S9d), considerably larger than those of PHC-0 and PHC-2. Combining with the N_2 and CO_2 sorption results, it could be

https://doi.org/10.1021/acs.nanolett.5c01616
Nano Lett. 2025, 25, 7161−7169

concluded that the PHC-2 mainly contains large open pores while the PHC-1 primarily contains small closed pores. These results strongly suggest that F127 plays a significant role in the pore structure of the hard carbon: an appropriate amount of F127 would induce the formation of small closed pores, while an excessive amount of F127 would lead to the formation of large open pores (Figure S10).

High-magnification HAADF-STEM images provide detailed insights into the local microstructure of PHC-1, particularly the graphitic layers and pore characteristics (Figure 2d). Statistical analysis of the images (Figure S11) reveal that the microcrystalline graphitic domains consist of approximately 3−4 stacked layers (Figure 2e) with an (002) interlayer spacing of ∼0.38 nm (Figure 2f). The closed pore size is centered at approximately 1.8 nm (Figure 2g).

While STEM images provide valuable information about the pore, they are inherently limited to two-dimensional projections, potentially obscuring the true nature of closed pores. To overcome this limitation and gain a comprehensive understanding of the closed pore structure of PHC-1, 3D electron tomography reconstruction is employed. A series of HAADF-STEM images are acquired at 2° intervals over a 150° angular range (see Figure 3a and Supplementary Video 1) and

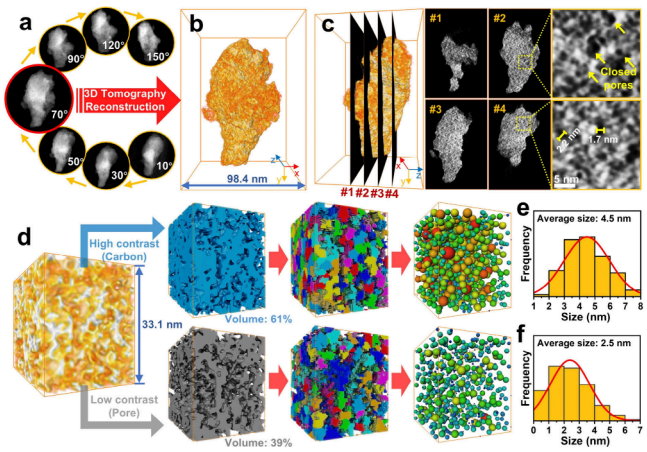

Figure 3. 3D structural reconstruction and pore structure analysis. (a) Representative HAADF-STEM images of the PHC-1 at different rotation angles; (b) reconstructed PHC-1 model; (c) side view (left), representative orthoslices from labeled positions (*xy* planes, perpendicular to the *z* axis, middle), and magnified orthoslices (right); (d) illustration of the subvolume segmentation by contrast, volume separation and generated network model (from left to right); and (e, f) statistical size distributions of the carbon (panel (e)) and the pore (panel (f)).

utilized for tomographic reconstruction. The reconstructed 3D model (Figure 3b) exhibited a shape consistent with the HAADF image at 70°, proving the authenticity of the reconstruction process. The front, top, and right views are displayed in Figure S12. To further illustrate the inner pore structure, 4 representative orthoslices are extracted from the labeled positions in the side view, revealing a uniform distribution of pores (∼2 nm) throughout the carbon (Figure 3c).

To gain further insight into the internal architecture of PHC-1, a cubic subvolume (23.9 nm × 29.6 nm × 33.1 nm) is extracted from the reconstructed tomographic model for quantitative analysis (indicated by the blue frame in Figure S12). Within this subvolume, contrast variations in the HAADF-STEM data, which arise from differences in atomic number (Z) and density, are utilized to segment the closed pores from the carbon matrix (Figure S13). In this context, the denser, higher-Z carbon matrix presents a brighter contrast than the less dense, lower-Z closed pores. Initial segmentation of HAADF-STEM uses different rendering to help audience visually distinguishing the target regions (carbon matrix rendered blue, pores as gray) (see Figure 3d and Supplementary Video 2). The volume fraction of closed pores is calculated to be ∼39% of the total subvolume. The volume separation module is employed to quantify pore and carbon segment morphology within the segmented subvolume. This tool applies a watershed algorithm to a distance map, delineating boundaries between adjacent yet topologically distinct features.[28]

Analysis of the separated objects yields an average closed pore size of 2.5 nm and an average carbon "building-unit" width of approximately 4.5 nm (see Figures 3e and 3f). The consistency between the pore size determined via tomography and that obtained from SAXS analysis underscores the reliability of both techniques for characterizing closed nanopores. While SAXS provides statistically averaged information over a larger sample volume, 3D tomography combined with HAADF-STEM offers visual confirmation and higher spatial resolution, therefore establishing a more comprehensive understanding of the porosity within the HC.

The electrochemical performances of the PHC samples are evaluated using cyclic voltammetry (CV) and galvanostatic charge−discharge (GCD) measurements. The CV curves for PHC-1 at 0.2 mV s^{-1} (Figure S14) exhibit a pair of sharp, symmetrical redox peaks at approximately 0.1 V, indicating highly reversible electrochemical reactions.[29]

The cycling performances at 50 mA g^{-1} are shown in Figure 4a. The PHC-1 demonstrates minimal capacity fade over 100 cycles, with a capacity retention of 90.6% (relative to the second cycle), significantly higher than those of PHC-0 (86.1%) and PHC-2 (82.2%). GCD profiles at 50 mA g^{-1} (Figure 4b) reveal that the PHC-1 achieves a reversible capacity of 361 mAh g^{-1} and an initial Coulombic efficiency (ICE) of 89%, outperforming both PHC-0 (295 mAh g^{-1}, 86% ICE) and PHC-2 (247 mAh g^{-1}, 81% ICE). The GCD profiles of all three samples exhibit the characteristic sloping region (>0.1 V) and plateau region (<0.1 V) typical of HC. Notably, PHC-1 displays a significantly enhanced plateau capacity compared to PHC-0 and PHC-2 (Figure 4c), which arises from its increased proportion of closed nanopores for Na deposition. The superior rate capability of PHC-1 is evident in Figure 4d. The PHC-1 consistently delivers higher capacities than PHC-0 and PHC-2 across all current densities tested (50−2000 mA g^{-1}). Even at 2000 mA g^{-1}, the PHC-1 retains a capacity of 230 mAh g^{-1}, and it recovers to 350 mAh g^{-1} when the current is reduced back to 50 mA g^{-1}. Long-term cyclability at 500 mA g^{-1} (Figure 4e) further demonstrates the exceptional stability of PHC-1, which exhibits a capacity retention of 90.7% after 500 cycles, significantly outperforming PHC-0 (79.1%) and PHC-2 (79.8%).

GITT measurements at a pulse current of 50 mA g^{-1} are used to calculate the Na^+ diffusion coefficients (D_{Na^+}) during both sodiation and desodiation. The PHC-1 exhibits higher D_{Na^+} values throughout both the sloping and plateau regions of the charge−discharge profile compared to those of PHC-0 and PHC-2 (Figure S15). EIS measurements (Figure S16) further reveal that PHC-1 has a charge transfer resistance (R_{ct})

https://doi.org/10.1021/acs.nanolett.5c01616
Nano Lett. 2025, 25, 7161−7169

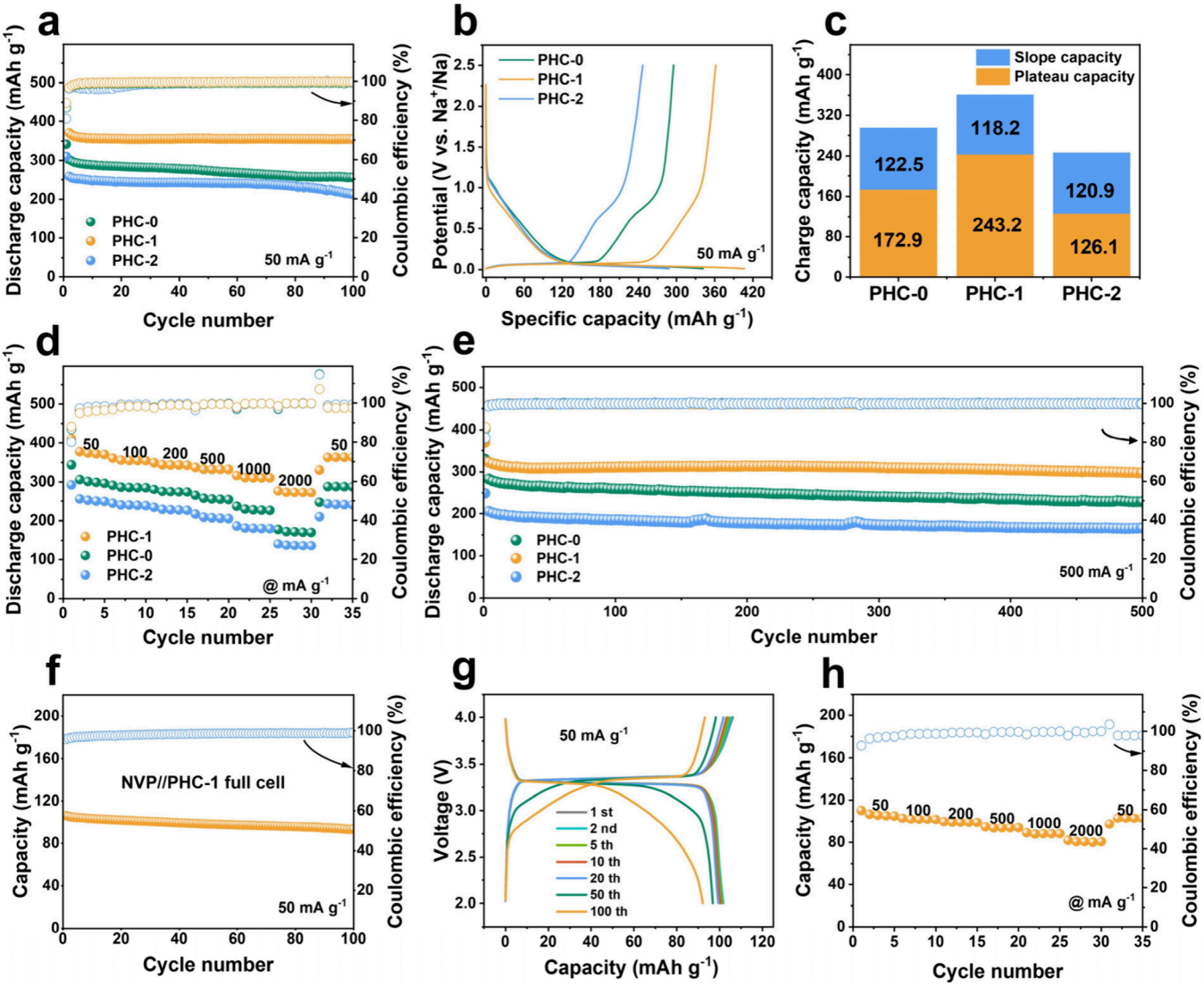

Figure 4. Electrochemical performance of PHC. (a) Cycling performances of PHC-0, PHC-1, and PHC-2 at 50 mA g^{-1}; (b) the first GCD profiles of PHC-0, PHC-1, and PHC-2; (c) the slope-region and plateau-region capacity contributions of PHC-0, PHC-1, and PHC-2 in the initial charge process; (d) rate performances of PHC-0, PHC-1, and PHC-2; (e) cycling performance of PHC-0, PHC-1, and PHC-2 at 500 mA g^{-1}; (f) cycling performance of the NVP//PHC-1 full cell at 50 mA g^{-1}; (g) GCD curves of the NVP//PHC-1 full cell; and (h) rate performance of the NVP//PHC-1 full cell.

significantly lower than those of PHC-0 and PHC-2. These findings indicate that the F127-templated pore structure in PHC-1 facilitates faster charge transfer and reduced polarization, ultimately enhancing the Na^+ transport kinetics.

Full cells are assembled using $Na_3V_2(PO_4)_3$ (NVP) as the cathode and PHC-1 as the anode. The NVP cathode exhibits excellent capacity and rate performance in a half-cell configuration (Figure S17). The NVP//PHC-1 full cell demonstrates a high reversible capacity of 102 mAh g^{-1} (based on the mass of NVP) at 50 mA g^{-1}, slightly lower than the capacity of NVP in the half-cell (Figure 4f). The full cell also achieves excellent cycling stability, retaining 90% of its initial capacity after 100 cycles at 50 mA g^{-1} (see Figures 4f and 4g). Furthermore, the NVP//PHC-1 full cell displays an impressive rate capability, maintaining a capacity of over 80 mAh g^{-1} even at 2000 mA g^{-1} (Figure 4h, Figure S18). These results demonstrate the excellent compatibility between PHC-1 and the NVP cathode, highlighting the significant potential of PHC-1 for practical applications.

In-situ XRD is employed to investigate the sodium storage mechanism of PHC-1 (Figure 5a). In the initial discharge within the sloping region, the (002) diffraction peak progressively narrows and its intensity diminishes. Based on previous studies, this behavior is attributed to the adsorption of Na^+ at defect sites, followed by Na^+ intercalation in graphitic carbon layers and the formation of NaC_x intercalation compounds.[30] Upon entering the plateau region, the (002) peak exhibits a minimal change, consistent with the filling of sodium into closed pores. This interpretation is further supported by the observed shift in binding energy of the ex-situ Na 1s XPS spectra (Figure S19), which demonstrates the formation of quasi-metallic sodium. During subsequent charging and in later cycles, the (002) peak broadens, and its intensity gradually recovers, signifying the reversibility of sodium storage process.[31]

In-situ Raman spectroscopy provides further insights into the structural evolution of PHC-1 during sodiation and desodiation (Figure 5b). During the initial discharging from

https://doi.org/10.1021/acs.nanolett.5c01616
Nano Lett. 2025, 25, 7161−7169

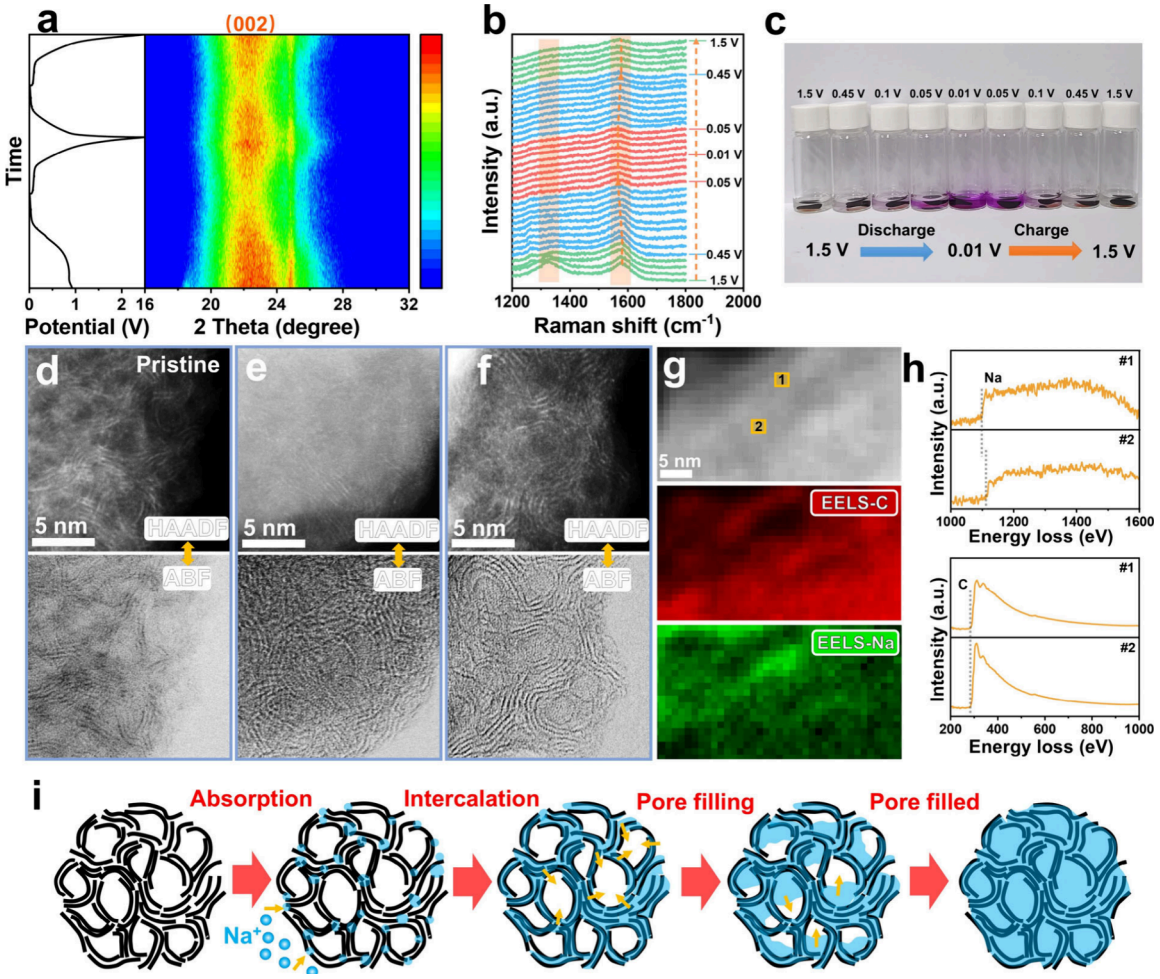

Figure 5. Sodium storage mechanism of PHC-1. (a) In-situ XRD spectra of PHC-1; (b) in-situ Raman spectra of PHC-1; (c) optical image showing the color change of ethanol containing 1 wt % phenolphthalein after reaction with the PHC-1 electrode at different potentials; (d, e, f) ex-situ HAADF/ABF-STEM of pristine PHC-1 (panel (d)), PHC-1 after discharged to 0.01 V (panel (e)), and PHC-1 charged to 2.5 V (panel (f)); (g) HAADF-STEM image and the corresponding EELS mappings of PHC-1 after discharged to 0.01 V; (h) EELS from areas marked "1" and "2" in panel (g); and (i) sodium storage mechanism diagram of the PHC-1.

1.5 V to 0.45 V, the G-band generally remains unchanged, while the D-band gradually broadens without a significant shift in position. This suggests that Na^+ adsorption primarily occurs at defect sites during the initial discharge process.[32] As the discharge continues to 0.05 V, a gradual shift of the G-band to lower frequencies is observed, indicating Na^+ intercalation into the carbon layers.[33] Upon further discharge to 0.01 V, both the G and D bands remain essentially unchanged, consistent with a pore-filling mechanism dominating this potential region.[34] During subsequent charging, the G-band shifts back to its original position, confirming the reversible nature of the structural changes associated with sodium storage.[35]

To probe the nature of sodium stored within PHC-1 during the low-voltage plateau, the disassembled electrodes are soaked in an ethanol solution containing 1 wt % phenolphthalein. The quasi-metallic sodium may react with ethanol to produce hydrogen gas and ethoxide, resulting in a characteristic color change in the presence of a phenolphthalein indicator.[16] As shown in Figure 5c, the ethanol solution remained colorless during the initial stages of discharge. However, upon reaching 0.1 V, a faint red color emerges, indicating the initial formation of quasi-metallic sodium within PHC-1. Further discharging to 0.01 V intensifies the red coloration and is accompanied by significant bubble evolution, suggesting more substantial formation of quasi-metallic sodium.

Ex situ AC-TEM with low-dose electron microscopy techniques is employed to further investigate the structural changes in PHC-1 during sodiation and desodiation. It is worth noting that low-dose electron microscopy techniques are typically employed to minimize beam-induced damage to sensitive materials such as Na clusters during imaging. In its initial state, the PHC-1 exhibits abundant closed pores (Figure 5d). Upon discharging to 0.01 V, both HAADF and ABF images (Figure 5e) show a marked reduction in the visibility of these closed pores, consistent with the filling of quasi-metallic sodium clusters within the nanopores.[36] This is further corroborated by EELS mapping (Figure 5g), which reveals a stronger Na signal within the pores of the discharged sample. Notably, a comparison of the Na EELS peak position in region 1 (pore interior) and region 2 (carbon matrix) shows a shift to lower energy in region 1 (Figure 5h), indicating an increased concentration of quasi-metallic sodium within the pores.[37] When charged back to 2.5 V, abundant closed pores reappear (Figure 5f), confirming the reversible defilling process. The (002) lattice spacing also exhibits reversible changes, expanding from 0.380 nm in the initial state to 0.389 nm

https://doi.org/10.1021/acs.nanolett.5c01616
Nano Lett. 2025, 25, 7161−7169

upon discharge to 0.01 V and contracting back to 0.383 nm after recharging to 2.5 V (Figure S20).

Based on the above observations, the sodium storage mechanism in PHC-1 can be described as a synergistic adsorption−intercalation−filling process, as illustrated schematically in Figure 5i. Initial storage involves Na adsorption on surfaces and defects, followed by intercalation between graphitic layers and, ultimately, the filling of closed pores with quasi-metallic sodium clusters.

This study leverages the capabilities of electron tomography to reconstruct in three dimensions the intricate porous architecture of PHC-1, providing quantitative data on porosity, pore size, and pore structure. AC-TEM with low-dose electron microscopy techniques is employed to directly visualize the spatial distribution of sodium clusters within the pores of PHC-1 after sodiation, providing unambiguous evidence of sodium deposition within these confined nanospaces. These advanced imaging techniques, coupled with comprehensive electrochemical characterization and complementary in-situ and ex-situ studies, allow us to elucidate the complex interplay between the pore architecture and the adsorption−intercalation−filling sodium storage mechanism. This work not only provides a thorough understanding of the sodium storage in the closed pores of HC but also provides insights into the rational design of advanced HC materials for SIBs.

■ ASSOCIATED CONTENT

Supporting Information

The Supporting Information is available free of charge at https://pubs.acs.org/doi/10.1021/acs.nanolett.5c01616.

FTIR spectra, TGA-DTG curves of PF and PF/F127; SEM images, TEM images, HAADF images, HRTEM images, XPS spectra, Raman spectrum, N_2 adsorption−desorption isotherms, SXAS patterns, CV profiles, GITT curves, EIS curves of PHC-0, PHC-1 and PHC-2; cycling performance, rate performance of $Na_3V_2(PO_4)_3$; GCD curves of the NVP//PHC-1 full cell; high-resolution Na 1s at different potentials, interlayer spacing at different potentials of PHC-1 (PDF)

Rotation and ortho slicing process of PHC-1 from 3D reconstruction (MP4)

Rotation and ortho slicing process of PHC-1 and voids components from contrast segmentation in 3D reconstruction (MP4)

■ AUTHOR INFORMATION

Corresponding Author

Liang Zhou − *The Sanya Science and Education Innovation Park, Wuhan University of Technology, Sanya 572000, The People's Republic of China; State Key Laboratory of Advanced Technology for Materials Synthesis and Processing, Wuhan University of Technology, Wuhan 430070, The People's Republic of China;* orcid.org/0000-0001-6756-3578; Email: liangzhou@whut.edu.cn

Authors

Bobo Sun − *The Sanya Science and Education Innovation Park, Wuhan University of Technology, Sanya 572000, The People's Republic of China; State Key Laboratory of Advanced Technology for Materials Synthesis and Processing, Wuhan University of Technology, Wuhan 430070, The People's Republic of China*

Ruohan Yu − *The Sanya Science and Education Innovation Park, Wuhan University of Technology, Sanya 572000, The People's Republic of China*

Yuxia Zhong − *The Sanya Science and Education Innovation Park, Wuhan University of Technology, Sanya 572000, The People's Republic of China; State Key Laboratory of Advanced Technology for Materials Synthesis and Processing, Wuhan University of Technology, Wuhan 430070, The People's Republic of China*

Jinshuai Liu − *The Sanya Science and Education Innovation Park, Wuhan University of Technology, Sanya 572000, The People's Republic of China; State Key Laboratory of Advanced Technology for Materials Synthesis and Processing, Wuhan University of Technology, Wuhan 430070, The People's Republic of China*

Zihe Wei − *The Sanya Science and Education Innovation Park, Wuhan University of Technology, Sanya 572000, The People's Republic of China; State Key Laboratory of Advanced Technology for Materials Synthesis and Processing, Wuhan University of Technology, Wuhan 430070, The People's Republic of China*

Xia Wang − *The Sanya Science and Education Innovation Park, Wuhan University of Technology, Sanya 572000, The People's Republic of China; State Key Laboratory of Advanced Technology for Materials Synthesis and Processing, Wuhan University of Technology, Wuhan 430070, The People's Republic of China*

Guangwan Zhang − *The Sanya Science and Education Innovation Park, Wuhan University of Technology, Sanya 572000, The People's Republic of China; State Key Laboratory of Advanced Technology for Materials Synthesis and Processing, Wuhan University of Technology, Wuhan 430070, The People's Republic of China*

Meng Huang − *The Sanya Science and Education Innovation Park, Wuhan University of Technology, Sanya 572000, The People's Republic of China;* orcid.org/0000-0003-4116-1348

Lei Zhang − *The Sanya Science and Education Innovation Park, Wuhan University of Technology, Sanya 572000, The People's Republic of China; State Key Laboratory of Advanced Technology for Materials Synthesis and Processing, Wuhan University of Technology, Wuhan 430070, The People's Republic of China*

Qin Wang − *Hubei Wanrun New Energy Technology Co., Ltd., Shiyan 442003, The People's Republic of China*

Fei Lv − *Hubei Wanrun New Energy Technology Co., Ltd., Shiyan 442003, The People's Republic of China*

Complete contact information is available at: https://pubs.acs.org/10.1021/acs.nanolett.5c01616

Author Contributions

The manuscript was written through contributions of all authors. All authors have given approval to the final version of the manuscript.

Author Contributions

▽Authors B. Sun and R. Yu contributed equally to this work.

Notes

The authors declare no competing financial interest.

■ ACKNOWLEDGMENTS

This work was supported by the National Natural Science Foundation of China (No. U23A20684).

REFERENCES

(1) Chen, Z.; Wu, X.; Sun, Z.; Pan, J.; Han, J.; Wang, Y.; Liu, H.; Shen, Y.; Li, J.; Peng, D.; Zhang, Q. Enhanced Fast-Charging and Longevity in Sodium-Ion Batteries through Nitrogen-Doped Carbon Frameworks Encasing Flower-Like Bismuth Microspheres. *Adv. Energy Mater.* **2024**, *14* (22), 2400132.

(2) Pan, J.; Sun, Z.; Wu, X.; Liu, T.; Xing, Y.; Chen, J.; Xue, Z.; Tang, D.; Dong, X.; Zhang, H.; Liu, H.; Wei, Q.; Peng, D.-L.; Amine, K.; Zhang, Q. Mechanically Robust Bismuth-Embedded Carbon Microspheres for Ultrafast Charging and Ultrastable Sodium-Ion Batteries. *J. Am. Chem. Soc.* **2025**, *147* (4), 3047−3061.

(3) Chen, X.; Liu, C.; Fang, Y.; Ai, X.; Zhong, F.; Yang, H.; Cao, Y. Understanding of the sodium storage mechanism in hard carbon anodes. *Carbon Energy* **2022**, *4* (6), 1133−1150.

(4) Nobuhara, K.; Nakayama, H.; Nose, M.; Nakanishi, S.; Iba, H. First-principles study of alkali metal-graphite intercalation compounds. *J. Power Sources* **2013**, *243*, 585−587.

(5) Kim, H.; Hong, J.; Yoon, G.; Kim, H.; Park, K.-Y.; Park, M.-S.; Yoon, W.-S.; Kang, K. Sodium intercalation chemistry in graphite. *Energy Environ. Sci.* **2015**, *8* (10), 2963−2969.

(6) Xu, Z.-L.; Yoon, G.; Park, K.-Y.; Park, H.; Tamwattana, O.; Joo Kim, S.; Seong, W. M.; Kang, K. Tailoring sodium intercalation in graphite for high energy and power sodium ion batteries. *Nat. Commun.* **2019**, *10* (1), 2598.

(7) Liu, J.; Huang, L.; Wang, H.; Sha, L.; Liu, M.; Sun, Z.; Gu, J.; Liu, H.; Zhao, J.; Zhang, Q.; Zhang, L. The Origin, Characterization, and Precise Design and Regulation of Diverse Hard Carbon Structures for Targeted Applications in Lithium-/Sodium-/Potassium-Ion Batteries. *Electrochem. Energy Rev.* **2024**, *7* (1), 34.

(8) Chu, Y.; Zhang, J.; Zhang, Y.; Li, Q.; Jia, Y.; Dong, X.; Xiao, J.; Tao, Y.; Yang, Q.-H. Reconfiguring Hard Carbons with Emerging Sodium-Ion Batteries: A Perspective. *Adv. Mater.* **2023**, *35* (31), 2212186.

(9) Shao, R.; Sun, Z.; Wang, L.; Pan, J.; Yi, L.; Zhang, Y.; Han, J.; Yao, Z.; Li, J.; Wen, Z.; et al. Resolving the Origins of Superior Cycling Performance of Antimony Anode in Sodium-ion Batteries: A Comparison with Lithium-ion Batteries. *Angew. Chem., Int. Ed.* **2024**, *63* (11), No. e202320183.

(10) Wang, F.; Jiang, Z.; Zhang, Y.; Zhang, Y.; Li, J.; Wang, H.; Jiang, Y.; Xing, G.; Liu, H.; Tang, Y. Revitalizing sodium-ion batteries via controllable microstructures and advanced electrolytes for hard carbon. *eScience* **2024**, *4* (3), 100181.

(11) Liu, J.; Huang, L.; Wang, H.; Sha, L.; Liu, M.; Sun, Z.; Gu, J.; Liu, H.; Zhao, J.; Zhang, Q.; Zhang, L. The Origin, Characterization, and Precise Design and Regulation of Diverse Hard Carbon Structures for Targeted Applications in Lithium-/Sodium-/Potassium-Ion Batteries. *Electrochem. Energy Rev.* **2024**, *7* (1), 34.

(12) Zeng, Y.; Yang, J.; Yang, H.; Yang, Y.; Zhao, J. Bridging Microstructure and Sodium-Ion Storage Mechanism in Hard Carbon for Sodium Ion Batteries. *ACS Energy Lett.* **2024**, *9* (3), 1184−1191.

(13) Wang, Z.; Feng, X.; Bai, Y.; Yang, H.; Dong, R.; Wang, X.; Xu, H.; Wang, Q.; Li, H.; Gao, H.; Wu, C. Probing the Energy Storage Mechanism of Quasi-Metallic Na in Hard Carbon for Sodium-Ion Batteries. *Adv. Energy Mater.* **2021**, *11* (11), 2003854.

(14) Sun, H.; Zhang, Q.; Ma, Y.; Li, Z.; Zhang, D.; Sun, Q.; Wang, Q.; Liu, D.; Wang, B. Unraveling the mechanism of sodium storage in low potential region of hard carbons with different microstructures. *Energy Storage Mater.* **2024**, *67*, 103269.

(15) Alvin, S.; Yoon, D.; Chandra, C.; Cahyadi, H. S.; Park, J.-H.; Chang, W.; Chung, K. Y.; Kim, J. Revealing sodium ion storage mechanism in hard carbon. *Carbon* **2019**, *145*, 67−81.

(16) Zheng, Z.; Hu, S.; Yin, W.; Peng, J.; Wang, R.; Jin, J.; He, B.; Gong, Y.; Wang, H.; Fan, H. J. CO2-Etching Creates Abundant Closed Pores in Hard Carbon for High-Plateau-Capacity Sodium Storage. *Adv. Energy Mater.* **2024**, *14* (3), 2303064.

(17) Huang, Y.; Zhong, X.; Hu, X.; Li, Y.; Wang, K.; Tu, H.; Deng, W.; Zou, G.; Hou, H.; Ji, X. Rationally Designing Closed Pore Structure by Carbon Dots to Evoke Sodium Storage Sites of Hard Carbon in Low-Potential Region. *Adv. Funct. Mater.* **2024**, *34* (4), 2308392.

(18) Wang, Y.; Yi, Z.; Xie, L.; Mao, Y.; Ji, W.; Liu, Z.; Wei, X.; Su, F.; Chen, C.-M. Releasing Free Radicals in Precursor Triggers the Formation of Closed Pores in Hard Carbon for Sodium-Ion Batteries. *Adv. Mater.* **2024**, *36* (26), 2401249.

(19) Zhang, X.; Cao, Y.; Li, G.; Liu, G.; Dong, X.; Wang, Y.; Jiang, X.; Zhang, X.; Xia, Y. Exploring Carbonization Temperature to Create Closed Pores for Hard Carbon as High-Performance Sodium-Ion Battery Anodes. *Small* **2024**, *20* (31), 2311197.

(20) Tang, Z.; Liu, R.; Jiang, D.; Cai, S.; Li, H.; Sun, D.; Tang, Y.; Wang, H. Regulating the Pore Structure of Biomass-Derived Hard Carbon for an Advanced Sodium-Ion Battery. *ACS Appl. Mater. Interfaces* **2024**, *16* (36), 47504−47512.

(21) Meng, Q.; Lu, Y.; Ding, F.; Zhang, Q.; Chen, L.; Hu, Y.-S. Tuning the Closed Pore Structure of Hard Carbons with the Highest Na Storage Capacity. *ACS Energy Lett.* **2019**, *4* (11), 2608−2612.

(22) Peng, L.; Peng, H.; Wang, S.; Li, X.; Mo, J.; Wang, X.; Tang, Y.; Che, R.; Wang, Z.; Li, W.; Zhao, D. One-dimensionally oriented self-assembly of ordered mesoporous nanofibers featuring tailorable mesophases via kinetic control. *Nat. Commun.* **2023**, *14* (1), 8148.

(23) Feng, S.; Li, K.; Hu, P.; Cai, C.; Liu, J.; Li, X.; Zhou, L.; Mai, L.; Su, B.-L.; Liu, Y. Solvent-Free Synthesis of Hollow Carbon Nanostructures for Efficient Sodium Storage. *ACS Nano* **2023**, *17* (22), 23152−23159.

(24) Sun, C.; Gao, F.; Wu, J.-Y.; Yang, Y.; Sun, Q. Microcrystalline cellulose-derived hard carbon for robust and low-potential sodium storage. *Carbon* **2025**, *232*, 119771.

(25) Wei, Z.; Zhao, H.-X.; Niu, Y.-B.; Zhang, S.-Y.; Wu, Y.-B.; Yan, H.-J.; Xin, S.; Yin, Y.-X.; Guo, Y.-G. Insights into the pre-oxidation process of phenolic resin-based hard carbon for sodium storage. *Mater. Chem. Front.* **2021**, *5* (10), 3911−3917.

(26) Song, Z.; Di, M.; Zhang, X.; Wang, Z.; Chen, S.; Zhang, Q.; Bai, Y. Nanoconfined Strategy Optimizing Hard Carbon for Robust Sodium Storage. *Adv. Energy Mater.* **2024**, *14* (43), 2401763.

(27) Reynolds, E. M.; Fitzpatrick, J.; Jones, M. O.; Tapia-Ruiz, N.; Playford, H. Y.; Hull, S.; McClelland, I.; Baker, P. J.; Cussen, S. A.; Pérez, G. E. Investigation of sodium insertion in hard carbon with operando small angle neutron scattering. *J. Mater. Chem. A* **2024**, *12* (29), 18469−18475.

(28) Youssef, S.; Rosenberg, E.; Gland, N.; Kenter, J. A. M.; Skalinski, M.; Vizika, O. High Resolution CT and Pore-Network Models to Assess Petrophysical Properties of Homogeneous and Heterogeneous Carbonates. In *SPE/EAGE Reservoir Characterization and Simulation Conference*, 2007; pp SPE-111427-MS.

(29) Chen, R.; Li, X.; Cai, C.; Fan, H.; Deng, Y.; Yu, H.; Mai, L.; Zhou, L. Amine−Aldehyde Condensation-Derived N-Doped Hard Carbon Microspheres for High-Capacity and Robust Sodium Storage. *Small* **2023**, *19* (44), 2303790.

(30) Cai, C.; Chen, Y.; Hu, P.; Zhu, T.; Li, X.; Yu, Q.; Zhou, L.; Yang, X.; Mai, L. Regulating the Interlayer Spacings of Hard Carbon Nanofibers Enables Enhanced Pore Filling Sodium Storage. *Small* **2022**, *18* (6), 2105303.

(31) Jiang, N.; Chen, L.; Jiang, H.; Hu, Y.; Li, C. Introducing the Solvent Co-Intercalation Mechanism for Hard Carbon with Ultrafast Sodium Storage. *Small* **2022**, *18* (15), 2108092.

(32) Bai, P.; He, Y.; Zou, X.; Zhao, X.; Xiong, P.; Xu, Y. Elucidation of the Sodium-Storage Mechanism in Hard Carbons. *Adv. Energy Mater.* **2018**, *8* (15), 1703217.

(33) Yin, X.; Lu, Z.; Wang, J.; Feng, X.; Roy, S.; Liu, X.; Yang, Y.; Zhao, Y.; Zhang, J. Enabling Fast Na+ Transfer Kinetics in the Whole-Voltage-Region of Hard-Carbon Anodes for Ultrahigh-Rate Sodium Storage. *Adv. Mater.* **2022**, *34* (13), 2109282.

(34) Anji Reddy, M.; Helen, M.; Groß, A.; Fichtner, M.; Euchner, H. Insight into Sodium Insertion and the Storage Mechanism in Hard Carbon. *ACS Energy Lett.* **2018**, *3* (12), 2851−2857.

(35) Gan, Q.; Qin, N.; Gu, S.; Wang, Z.; Li, Z.; Liao, K.; Zhang, K.; Lu, L.; Xu, Z.; Lu, Z. Extra Sodiation Sites in Hard Carbon for High

https://doi.org/10.1021/acs.nanolett.5c01616
Nano Lett. 2025, 25, 7161−7169

Performance Sodium Ion Batteries. *Small Methods* **2021**, *5* (9), 2100580.
(36) You, S.; Zhang, Q.; Liu, J.; Deng, Q.; Sun, Z.; Cao, D.; Liu, T.; Amine, K.; Yang, C. Hard carbon with an opened pore structure for enhanced sodium storage performance. *Energy Environ. Sci.* **2024**, *17* (21), 8189−8197.
(37) Ji, T.; Liu, X.; Wang, T.; Shi, Y.; Sheng, D.; Hao, X.; He, C.; Shen, Z. Commercial Carbon Fibers as Host for Sodium Deposition to Achieve High Volumetric Capacity. *Adv. Funct. Mater.* **2024**, *34* (49), 2408880.

https://doi.org/10.1021/acs.nanolett.5c01616
Nano Lett. 2025, 25, 7161−7169